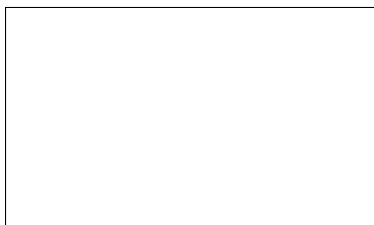**Phase stability of the layered oxide, Ca2Mn3O8: probing the pressure-temperature phase diagram**

Vera-Stimpson, L., Etherdo-Sibley K. J., Ridley C. J., Bull C. L. and Arnold D. C

Graphical Abstract

Phase stability of the layered oxide, $Ca_2Mn_3O_8$; probing the pressure-temperature phase diagram

Laura J. Vera Stimpson,Kevin J. W. Etherdo-Sibley,Christopher J. Ridley,Craig L. Bull,Donna C. Arnold

Highlights

Phase stability of the layered oxide, $Ca_2Mn_3O_8$; probing the pressure-temperature phase diagram

Laura J. Vera Stimpson,Kevin J. W. Etherdo-Sibley,Christopher J. Ridley,Craig L. Bull,Donna C. Arnold

- First high pressure study of $Ca_2Mn_3O_8$

- Insight into the compression mechanism of $Ca_2Mn_3O_8$

- Comparison of compressibility at temperatures of $290\,K$ and $120\,K$

Phase stability of the layered oxide, $Ca_2Mn_3O_8$; probing the pressure-temperature phase diagram

Laura J. Vera Stimpson[a,b], Kevin J. W. Etherdo-Sibley[a], Christopher J. Ridley[c], Craig L. Bull[c,*] and Donna C. Arnold[a,*]

[a]*School of Physical Sciences, University of Kent, Canterbury, Kent, CT2 7NH, UK*
[b]*Faculty of Social and Applied Sciences, Canterbury Christ Church University, Canterbury, Kent, CT1 1QU, UK*
[c]*ISIS Neutron and Muon Source, Rutherford Appleton Laboratories, Chilton, Didcot, OX11 0QX, UK*

ABSTRACT

We have performed high–pressure neutron diffraction studies on the layered oxide, $Ca_2Mn_3O_8$. Studies up to approximately 6 GPa at temperatures of 120 and 290 K demonstrate that there are no structural phase transitions within this pressure range. Fits of the unit–cell volume to a Birch-Murngaham equation of state give values for the bulk modulus of 137(2) GPa and 130(2) GPa at temperatures of 290 K and 120 K respectively suggesting that $Ca_2Mn_3O_8$ is more compressible at lower temperature. Compression along the principle axes are anisotropic on the local scale with comparison of individual bond lengths and bond angle environments demonstrating that compression is complex and likely results in a shearing of the layers.

1. Introduction

Layered metal oxides continue to attract extensive attention due to their large compositional flexibility and wide variety of potential applications. The prototypical layered transition metal materials are the delafossite family typified by the formulae ABO_2 (where A is a monovalent cation such as Na^+ or Cu^+, B is a trivalent transition metal such as Fe^{3+} or Mn^{3+}. The structure can be described by BO_6 layers separated by A^+ cations. As a result applications in renewable energy [1, 2, 3, 4, 5, 6, 7] and catalysis [8, 9, 10] have been reported. Furthermore, the triangle connectivity between the transition metal species means that exotic magnetic states can be realised when B is a magnetic species [11, 12, 13, 14, 15, 16].

We have become interested in the delafossite related material, $Ca_2Mn_3O_8$. $Ca_2Mn_3O_8$ crystallises in a monoclinic $C2/m$ layered structure which can be described by $Mn_3O_8{}^{4-}$ sheets, formed from edge sharing MnO_6 octahedra, separated by trigonal bipyramidal CaO_6 sites as shown in figure 1 [17, 18, 19]. In contrast with delafossites, these materials have a nominal formulae of $Ca_{0.5}Mn_{0.75}O_2$ as a result the B-site cation layers are incomplete with a quarter of the triangular lattice sites (Mn^{4+} octahedral) vacant. This leads to a network of ordered voids within the 2D layers realising a '*bowtie*' connectivity of the Mn_{4+} ions (Figure 1) [17, 18, 19]. The location of this void alternates between layers giving rise to *ABAB* stacking in the lattice a-direction [17, 18, 19]. The same authors later characterised the magnetic behaviour of the material as antiferromagnetic from SQUID magnetometry [20]. As with delafossite materials, $Ca_2Mn_3O_8$ has

been investigated for the catalytic splitting of water [21, 22, 23, 24, 25, 26, 27] and as a potential battery electrode [28]. However, the understanding of the structure-property relationships in this material has been limited by the low crystallinity of the as synthesised materials. We have previously demonstrated that the synthetic route can have a large effect on the morphology observed with solid–state methods giving large spherical particles comprised of small crystallites, sol-gel methods producing nano-sized particles and hydrothermal methods yielding flake-like geometries with large surface areas [29]. However, all synthetic routes led to materials with low crystallinity making further analysis difficult. Recently, we developed a molten salt synthetic route which allowed us to synthesis high quality $Ca_2Mn_3O_8$ bulk materials [30]. The high quality of these materials allowed us to perform more comprehensive studies of the thermal stability and magnetic behaviour of this material [30, 31]. Low temperature studies (1.8 – 300 K) showed that $Ca_2Mn_3O_8$ orders antiferromagnetically with an ↑↑↓↓ spin arrangement of magnetic spins at a Néel temperature (T_N) of approximately 58 K [30]. Additionally, an invariant behaviour below 130 K is seen in the lattice parameter, b and the monoclinic β angle. This occurs at the same temperature as a deviation from Curie Weiss behaviour is observed and is consistent with short-range spin correlations [30]. Data collected between 300 and 1273 K shows that the monoclinic structure is remarkably stable up to a temperature of approximately 1200 K before it decomposes into the perovskite, $CaMnO_3$ and marokite, $CaMn_2O_4$ phases [31]. Moreover, electrical measurements confirm the $Ca_2Mn_3O_8$ is an electronic conductor in the temperature range of 400 - 700 K with an activation energy of 0.50(1) eV [31].

Given the interesting nature of $Ca_2Mn_3O_8$ and the stability of the $C2/m$ structure as a function of temperature it is of interest to determine the distortion of this structure on the application of hydrostatic pressure. Applied pressure is
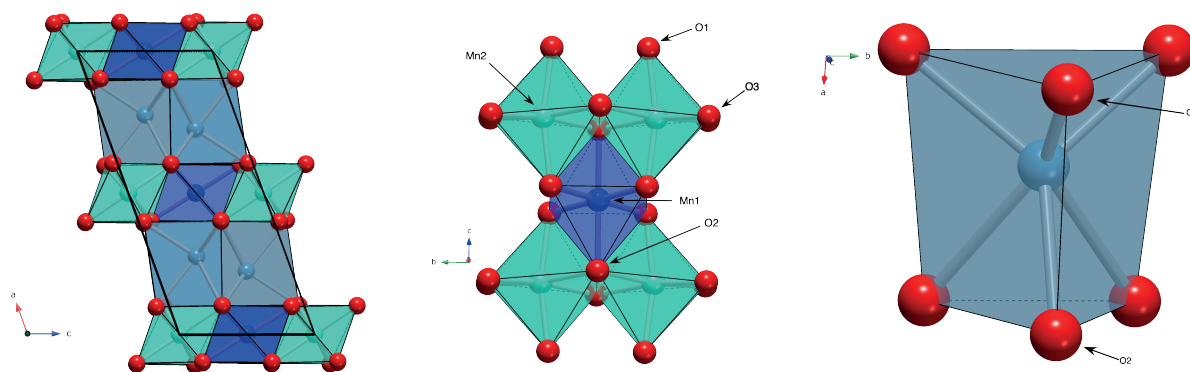
Figure 1: Schematic representation of the Ca$_2$Mn$_3$O$_8$ structure showing, left:the MnO$_6$ edge shared layers separated by CaO$_6$ trigonal bipyramids. Note the calcium position alternates due to *ABAB* stacking resulting from the shifting structural void position between subsequent layers. Middle: Edged shared MnO$_6$ octahedra connectivity forming the '*bow-tie*' like connectivity of the Mn^{4+} ions and Right: CaO$_6$ trigonal bipyramidal unit showing the aniostropic nature of the polyhedra arising as a result of the alternating position of the void. The dark blue spheres and squares represent the Mn^{4+} ion and MnO$_6$ octahedra on the Mn1 crystallographic site, the green spheres and squares represent the Mn^{4+} ion and MnO$_6$ octahedra on the Mn2 crystallographic site, the light blue spheres and squares represent the Ca^{2+} ion and CaO$_6$ trigonal bipyramids and the red spheres represent the oxygen ions respectively

an effective way to change co–ordination environments and tune property behaviour driving very different distortion behaviour upon increasing pressure. for example, in the perovskite family of materials there are examples of both decreasing and increasing structural distortions which are controlled by the relative compressibilties of the two types of polyhedra present within the structure [32]. A number of compressability studies (both experimental [33, 34, 35, 36, 37, 38, 39, 40, 41, 42, 43, 44, 45, 46] and computational [47, 48, 49, 50]) have been performed on CuFeO$_2$ and related rhombohedral ($R\bar{3}m$) delafossites. Structural studies show that the compression of the lattice is anisotropic with the compressability within the lattice c direction (between the layers) being far larger than that of the lattice a direction (within the layers) [40, 41, 42, 43, 44, 45]. In CuFeO$_2$ the $R\bar{3}m$ structure has been shown to be stable up to pressure of approximately 18 GPa before transformation to a monoclinic, $C2/c$ phase [42]. At approximately 23 GPa there is a second partial transformation of the structure to a trigonal $P\bar{3}m$ phase resulting from interatomic valence change from Cu^{1+}/Fe^{3+} sites in the low pressure phases to a Cu^{2+}/Fe^{2+} phase above 23 GPa [42]. In contrast in CuGaO$_2$ and CuAlO$_2$ the $R\bar{3}m$ structure is stable up to a pressures of 28 GPa and 35 GPa respectively [40, 43]. Above this pressure there is an irreversible phase transition to an unidentified phase which seems to be driven primarily by the Cu site. The pressure dependent magnetism has been extensively studied in CuFeO$_2$ [33, 34, 35, 36, 37, 38, 39, 46]. At ambient pressure CuFeO$_2$ exhibits two distinct antiferromagnetically ordered states [46]. At 14 K (T_{N1}) the spins order with a incommensurately modulated collinear spin density wave [46]. Below 11 K (T_{N2}) this turns into a collinear commensurate four sub-lattice (4SL, ↑↑↓↓) ordering [46]. At the same time there is a lowering of the symmetry from rhombohedral to monoclinic. With applied pressure the transition temperature of the spin density

wave (T_{N1}) increases [46]. In contrast the behaviour below T_{N2} is far more complex. With increasing pressure the transition temperature falls slightly and a number of pressure induced magnetic phase transitions occur. Firstly, a transition to an incommensurately modulated proper screw ordered state at approximately 3 GPa. This is followed by a transition to an incommensurate state which has signatures of both cycloidal and proper screw configurations and finally to the high temperature incommensurate spin density wave (i.e. there is only a single magnetically ordered state at high pressures) at pressures of approximately 4 GPa and 6 GPa respectively [46]. More recently, more complex magnetic correlations as a function of both applied pressure and magnetic field have been reported [51].

In this paper we demonstrate by neutron powder diffraction that there are no pressure induced structural phase transitions up to a pressure of 6 GPa at temperatures of 290 and 120 K in Ca−2Mn$_3$O$_8$. Compression behaviour is shown to be complex and largely results from a shearing of the layers.

2. Materials and Method

2.1. Sample Synthesis and Characterisation

Ca$_2$Mn$_3$O$_8$ was synthesised using a molten salt method as previously reported by us [30]. Briefly, stoichiometric ratios of CaCO$_3$ (Sigma Aldrich, ≥99%), MnCO$_3$ (Sigma Aldrich, ≥99%) and a eutectic mixture of KCl/NaCl (350% (w/w)) were mixed and reacted for 48 hours at 973 K (ramp rate 10 Kmin^{-1}) followed by a second heating cycle of 24 hours at 973 K (ramp rate 10 Kmin^{-1}). After both heating cycles, the material was quenched to room temperature. Between heating cycles the material was washed and dried under ambient conditions and an additional 350% (w/w) eutectic mixture of KCl/NaCl was added for the second heating.

Phase purity was confirmed using a Rigaku Miniflex 600 powder X-ray diffractometer (40 kV and 15 mA, with λ=

1.5406 Å) over a 2θ range of 10° to 70° (data not shown here).

2.2. High–Pressure Diffraction

Neutron Powder Diffraction (NPD) data were collected under applied pressures of 0–6 GPa at room temperature and 0–5 GPa at 120 K, using the PEARL diffractometer at the ISIS Neutron and Muon Facility (UK) [52]. A powdered sample of Ca$_2$Mn$_3$O$_8$ was loaded into toroidal profile anvils machined from zirconia toughened alumina, encapsulated in a null scattering TiZr gasket and sealed in the Paris–Edinburgh press with an applied load of 6 tonnes [53, 54]. Time–of–flight neutron powder diffraction patterns were collected in ~1 GPa increments for ~ 4 hours each. Data was focused, normalised and intensity corrected for anvil attenuation using in house software [52, 55]. Rietveld refinements were performed using the GSAS suite of programs (full details are provided in the electronic supplimentary information) [56, 57]. The data collection at 120 K was performed in the same manner except the Paris-Edinburgh press was cooled using a modified Paris–Edinburgh press with liquid N$_2$ cooling rings and described elsewhere [52]. In both experiments a small piece of lead was included in the gasket chamber and used as a pressure marker and a 4:1 (by volume) mix of perdueterated methanol:ethanol was used to ensure compression was made under hydrostatic conditions [58, 59].

3. Results and Discussion

Figure 2 shows the time–of–flight diffraction pattern of Ca$_2$Mn$_3$O$_8$ as collected on the PEARL instrument at the sealing load of 6 tonnes in the Paris–Edinburgh press. The associated Rietveld refinement is also shown. Table 1 shows the results of the Rietveld refinement and the results compared to those published previously [17]. The data clearly indicated an excellent fit to the monoclinic, C2/m, model expected for Ca$_2$Mn$_3$O$_8$ [17, 30, 31]. Additional phases of Pb (Fm$\bar{3}$m) from the pressure calibrant, and ZrO$_2$ (P4$_2$/nmc) and Al$_2$O$_3$ (R$\bar{3}$c) from the anvil were also refined.

Upon increasing pressure at both 290 and 120 K there is no change in diffraction pattern beyond that expected with increasing pressure. Rietveld refinement of the structural model permits the lattice parameters of the monoclinic cell to be determined and with increasing pressure they show a continuous decrease as shown in Figure 3. We find no evidence for a change in symmetry (at either 120 or 290 K) and thus conclude that the C2/m crystal symmetry is maintained up to the highest pressure studied (~6 GPa). This is consistent with studies on related delafossite materials which are also seen to be stable over this pressure range [40, 41, 42, 43, 44, 45]. Refinement profiles and data tables are provided in the ESI for data collected at all pressure points. There is a clear difference in the rate of compression of the three crystallographic axes as a function of temperature. The a- and b-lattice parameter shows no difference in compression rate irrespective of temperature. However, the c-axis shows a greater compression rate at 120 K when compared to the 290 K data as shown by the change in slope (Figure
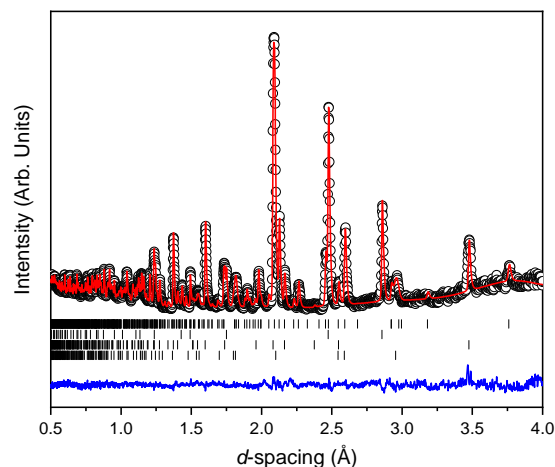

Figure 2: Rietveld refinement of the room temperature data collected for Ca$_2$Mn$_3$O$_8$ as loaded in the Paris-Edinburgh high pressure cell. The black circles represent the data collected, the red line the calculated model and the blue trace the difference between the two. The vertical tick marks indicate the predicted peak positions for (top to bottom) the Ca$_2$Mn$_3$O$_8$ phase, Pb pressure marker, the Al$_2$O$_3$ and ZrO$_2$ phases of the anvils.
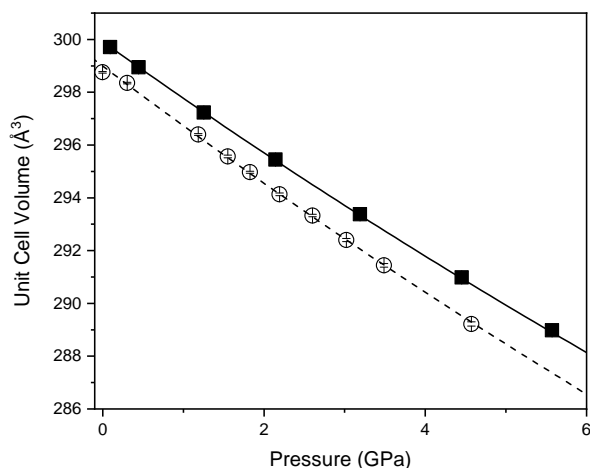
Table 1

Details of structural parameters determined from Rietveld refinement of Ca$_2$Mn$_3$O$_8$. Data collected at 0.09 GPa within the Paris–Edinburgh press and compared to that collected previously by single-crystal x-ray diffraction by Ansell *et al*[17]. Determined lattice parameters, unit–cell volume (V) and refined atomic coordinates as shown for the Ca atom on the 4i site with y=0, Mn1 on the 2c site with x=y=0, z=$\frac{1}{2}$, Mn2 on the 4g site x=z=0, O1 on the 8j site, O2 on the 4i site y=$\frac{1}{2}$ and O3 on the 4i site y=0.

Parameter	This Study	Previous Study[17]
a (Å)	11.0212(6)	11.014(4)
a (Å)	5.8465(3)	5.851(3)
a (Å)	4.9428(3)	4.942(2)
β (°)	109.785(4)	109.73(5)
V (Å^3)	299.707(3)	299.78
Ca x,z	0.722(6),0.6613(12)	0.72442(3),0.66593(7)
Mn2 y	0.25100(15)	0.25914(4)
O1 x,y	0.0980(4)0.2220(6)	0.10059(7), 0.22158(15)
O1 z	0.3894(8)	0.39171(17)
O2 x,z	0.5955(6),0.08918(12)	0.59726(11), 0.90202(25)
O3 x,z	0.6042(5),0.9585(10)	0.60385(11), 0.96258(26)
wRp, χ^2	2.43,1.027	3

3). This is also seen significantly in the behaviour of the monoclinic unit–cell angle (β). The beta angle is decreasing form initial values of 109.785(4)° and 109.745(4)° at 290 and 120 K respectively at ambient pressure to 109.750(5)° and 109.671(13)° at 290 and 120 K and pressures of 5.6 GPa and 4.6 GPa respectively suggesting that the lattice is more
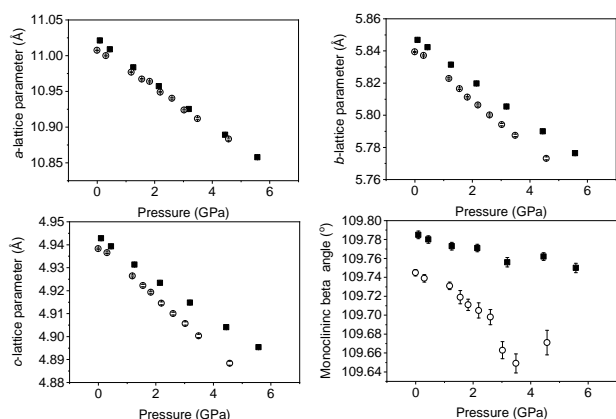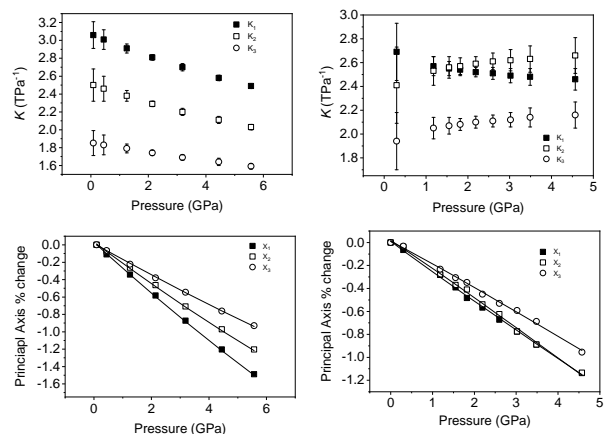
Figure 3: Variation of Ca$_2$Mn$_3$O$_8$ lattice parameters as a function of pressure. Top left: *a*-lattice parameter Top Right: *b*-lattice parameter, Bottom Left: the *c*-lattice parameter and Bottom Right: the beta angle. The filled symbols represent the compression data collected at 290 K and the open symbols represent the compression data collected at 120 K compression.

Figure 5: Pressure dependent behaviour of the median compressibilties (K$_n$) of the principal axes (X$_n$). Top left: at 290 K. The filled squares correspond to the K$_1$, the open squares the K$_2$ and the open circles the K$_3$ compressibilities in the X$_1$, X$_2$ and X$_3$ principle directions. Top right: at 120 K. The filled squares correspond to the K$_1$, the open squares the K$_2$ and the open circles the K$_3$ compressabilities in the X$_1$, X$_2$ and X$_3$ principle directions. Bottom left: percentage change in the principle axes at 290 K. The filled squares correspond to the X$_1$, the open squares the X$_2$ and the open circles the X$_3$ principle directions. Bottom right: percentage change in the principle axes at 120 K. The filled squares correspond to the X$_1$, the open squares the X$_2$ and the open circles the X$_3$ principle directions.

Figure 4: Variation of unit cell volume as a function of pressure showing a smooth decrease with increasing pressure. The filled symbols represent the compression data collected at 290 K and the open symbols represent the compression data collected at 120 K compression.

with a pressure derivative of 4.5(5) (Table 2). Such a bulk modulus is comparable with other layered oxides such as CuFeO$_2$ (156 GPa and 2.6) [44, 45], CuFeO$_2$ (140 GPa and 4) [42], PbCoO$_2$ (225 GPa and 0.7) and CuGaO$_2$ (202 GPa and 3.9) [40]. In Ca$_2$Mn$_3$O$_8$ there is a small decrease in the bulk modulus upon cooling to 120 K (Table 2). Furthermore, it is clearly evident that the compressibility behaviour is very different at 290 and 120 K (Figure 3).

We have established that upon compression at 290 and 120 K there is no change in crystal symmetry of Ca$_2$Mn$_3$O$_8$ with increasing pressure. However, compression behaviour can only be understood directly from unit cell dimensions when they are orthogonal, i.e. when they lie coincident with the principal axes of the strain tensor. For non-orthogonal axes (as is the case here), these must be reformulated into a Cartesian set. We have determined the principal axes (their relation to the unit-cell axes), and their corresponding compressibilities [60], for both temperatures. Table 2 shows determined bulk modulus (B$_0$) and median compressibilties (K$_n$) of the principal axis (X$_n$). It can be seen that the compressability is anisotropic which is consistent with that reported for rhombohedral ($R\bar{3}m$) delafossite materials [40, 41, 42, 43, 44, 45]. The median compressibilities of the principal axis with a predominant a direction (X$_1$ and X$_2$ at 290 and 120 K respectively) show very similar median compressibilties (K$_1$ and K$_2$) (as reflected in Figure 5. For the principal axis with predominant *b*-axis (K$_2$ and K$_1$ at 290 and

compressible at low temperature. Overall the structure is becoming less distorted with increasing pressure as suggested by the decrease in monoclinic cell angle (β) consistent with what has been observed in layered delafossite materials [40].

Figure 5 shows the variation of the unit-cell volume with increasing pressure at 290 and 120 K. It shows that at both temperatures the cell volume decreases smoothly with increasing pressure indicating no structural changes consistent with lattice parameter behaviour. The variation of the volume has been fitted with a Birch-Murngaham equation of state. At 290 K the determined bulk modulus is 136.8(20) GPa

120 K respectively the compressibility increases upon cooling) with the same trend seen for the *c*-axis direction (K$_3$ for 290 and 120 K). At 290 K the three principal axis all show very different median compressibilties to each other. However, at 120 K the values of K$_1$ and K$_2$ are similar in value. The actual compressibilites of all axis decrease with increasing pressure at 290 K however as seen in Figure 5 the compressibilties of K$_2$ and K$_3$ increase with increasing pressure. The fact that some median compressibilties increase upon cooling suggest that some changes must occur to the structure or electronic properties determining the bond strength upon cooling. This could possibly be related to short range mangnetic correlations which are known to propagate at temperatures below approximately 130 K at ambient pressure [30]. In order to understand this further the behaviour of the individual bond lengths and polyhedra need to be understood upon compression.

Table 2

Values derived from the Birch-Murngaham equation of state fit to the unit cell volume and the compressability of the principle axes (determined using reference [60]) at both 290 and 120 K. *A second order fit is made to the the 120 K data set with an implied B' value of 4.

Parameter	290 K	120 K
V$_0$ (Å^3)	299.92(5)	298.99(6)
B$_0$ (GPa)	137(2)	130(2)
B'	4.5(5)	4*
K$_1$ of X$_1$	2.49(2)	2.51(5)
Direction of X$_1$	$\approx 0.97a + 0.3c$	$= b$
K$_2$ of X$_2$	2.03(3)	2.61(7)
Direction of X$_2$	$= -b$	$\approx -0.8a + 0.6c$
K$_3$ of X$_3$	1.59(3)	2.11(5)
Direction of X$_3$	$\approx c$	$\approx -0.3a - c$

Figure 6 shows the variation in the average Mn-O bond lengths in the two crystallographically distinct MnO$_6$ octahedra. Both octahedra (Mn1 and Mn2) display a decrease in the average bond length and individually the bond lengths within the octahedra show the same behaviour (see ESI). The average Mn(2)O$_6$ bond lengths show a greater compressibilty than that of the Mn(1)O$_6$ (Figure 6). This behaviour is also reflected in the rate of change of the polyhedral volume with pressure (Figure 6); the volume of the Mn(1)O$_6$ polyhedra decreases at a lower rate compared to that of the larger Mn(2)O$_6$ polyhedra. However, for both polyhedra no measurable change in distortion is seen. Within the Mn(1)O$_6$ octahedra there is a clear contraction of the Mn1–O1 bond lengths which lie in the *a–b* plane (see ESI). In contrast for the most part there is little change in the Mn1–O2 bond lengths, which predominantly lie in the lattice *c* plane within this octahedral unit (Figure 1). There is a decrease in the Mn2–O1 bond length with increasing pressure however, we see very little change in the Mn2–O3 bond lengths (see ESI). We note that Mn2–O1 and Mn2–O3 bonds predominantly lie in the lattice *a–b* plane. Likewise, we see a change in the Mn2–O2 bond lengths (lying predominantly in the lattice *c*-direction)

with increasing pressure. There is very little change in the Mn–O–Mn bond angles suggesting there is no rotation of the MnO$_6$ octahedra or buckling of the layers. Additionally, whilst both octhahedral sites contribute to lattice contraction in the *a* and *b* directions only the Mn(2)O$_6$ octahedra drives the contraction of the layers in the lattice *c* direction. This is perhaps not surprising given that the MnO$_6$ octahedra are edge-shared within the layers and is consistent with the relatively small change in dimensions seen in the *c*-direction when compared to the *a*- and *b*-directions.

As described previously, in Ca$_2$Mn$_3$O$_8$, the calcium cation is sited between the MnO$_6$ layers within a six coordinate trigonal bipyramidal site as shown in figure 1. The contraction of these bonds is a little more complex with all three bond lengths (Ca–O1, Ca–O2 and Ca–O3) contributing to lattice contraction in all three crystallographic directions. The average Ca–O bond length (shown in Figure 6) decreases with increasing pressure. The rate of decrease is greater than the Mn–O bond contraction. Also Figure 6 shows a significant decrease in CaO$_6$ polyhedral volume with increasing pressure.

Looking at the individual Ca–O bonds within the polyhedra, there is little change in the Ca-O1 bond length with increasing pressure whilst both the Ca-O2 and Ca-O3 bond lengths show a clear contraction. This would seem to suggest that the CaO$_6$ polyhedra become increasingly distorted with increasing pressure. Previous work using the difference in the bond valence sum (ΔV_i) has suggested that a value of > 0.1 is a result of strain within a polyhedra [32]. ΔV_i for the CaO$_6$ polyhedra shows a clear increase in value with increasing pressure (Figure 6). Indeed for the CaO$_6$ polyhedra the initial value is 0.2 and this doubles upon application of a pressure of ∼6 GPa. This is in contrast with the behaviour of the MnO$_6$ polyhedra where the Mn(2)O$_6$ shows no real strain or changes with increasing pressure and only the Mn(1)O$_6$ polyhedra show an increase in strain suggested by the bond valence difference from 0.28 to 0.4 at 5.6 GPa.

In contrast with the Mn–O–Mn bond angles there are systematic changes in the bond angles associated with the calcium site (as shown in the ESI). The Ca–O1–Ca bond angle shows a small increase with increasing pressure. This effectively acts to pull the layers closer together as shown in figure 7. The layer stacking in Ca$_2$Mn$_3$O$_8$ is *ABAB* with the interlayer voids formed within the MnO$_6$ framework shifted with respect to each other in adjacent layers [29, 17, 19, 18, 20, 30, 31]. This means the Ca–O–Mn bond environments are different above and below the Ca^{2+} cation as shown in figure 7. These environments also alternate as you move between Ca^{2+} cations within the layer. The Ca–O1–Mn1 and Ca–O1–Mn2 bond angles are each described by two different values depending on if the angle describes bond angles linked to the 'top' or 'bottom' layer (as is depicted in the arrangement in figure 7). In fact all bond angles associated with the top layer (Ca-O1-Mn1, Ca-O1-Mn2 and Ca-O3-Mn2) all show little change with increasing pressure. In contrast those bond angles associated with the bottom layer show consistent changes with increasing pressure. In addi-
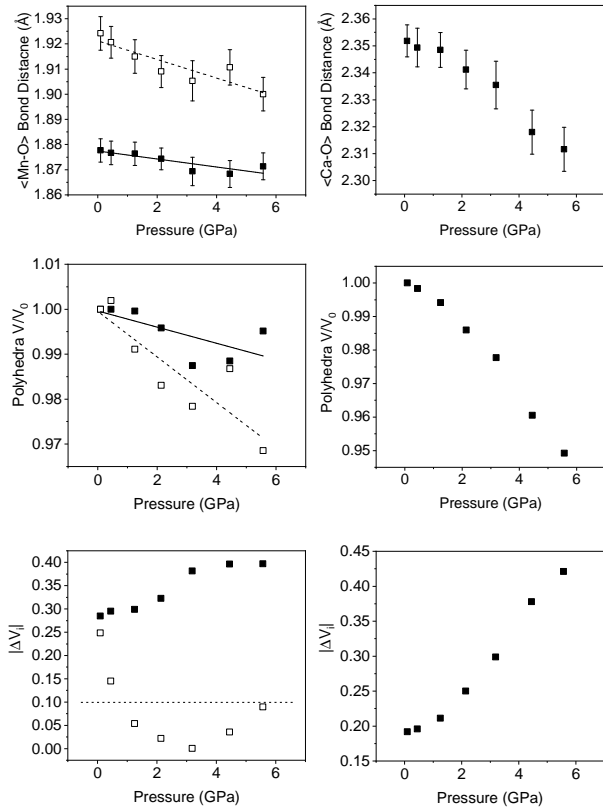
Figure 6: Variation in polyhedral and associated bond behaviour of Ca_2MnO_8 with increasing pressure at 290 K. Top Left: Average bond lengths in the two MnO_6 octahedra $Mn(1)O_6$ (solid squares) and $Mn(2)O_6$ (open squares). The lines show best fit through the data points. Top Right: Average bond length of the CaO_6 trigonal bipyramidal site. Middle Left: Normalsed MnO_6 octahedra volume of $Mn(1)O_6$ (filled squares) and $Mn(2)O_6$ (open squares). The lines show best fit through the data points. Middle Right: Normalised CaO_6 trigonal bipyramidal polyhedral volume. Bottom Left: Bond valence difference of the $Mn(1)O_6$ and $Mn(2)O_6$ octahedra. The dashed line shows the value above which the difference is thought to be a result of bond strain among the bonds between the cation and surrounding anions. Bottom Right: Bond valence difference of the CaO_6 trigonal bipyramidal polyherdra.

KEY

tion to the decreasing bond angle trends described above for Ca-O1-Mn1 and Ca-O1-Mn2, the Ca-O2-Mn2 and Ca-O2-Mn1 (non-bonding) bond angles both subtly increase with increasing pressure. This suggests that a shearing (consistent with the decrease of the β angle) of the layers contributes to the contraction in the lattice a-direction. This is consistent with the larger contractions seen in the interlayer dimensions seen in the delafossites (in this case the lattice c direction) [40, 43, 42, 41, 45, 45].
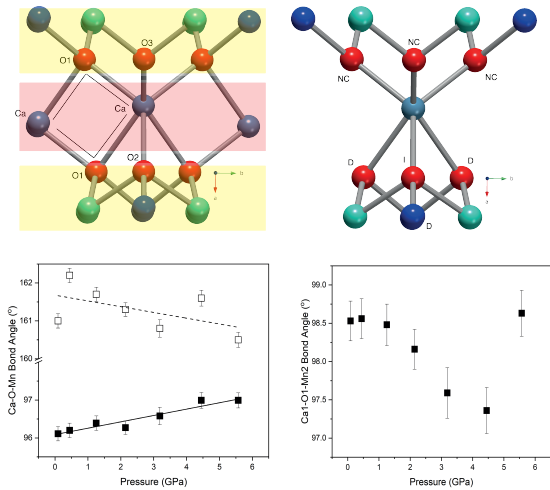
Figure 7: Schematic representation Top Left: of Ca–O1–Ca bond angles showing that these represent movement between the MnO_6 layers, the red shading representing the A layer and the yellow shading the B layer (see text for details) and Top Right: Mn–O–Ca bond angles showing that those angles above the calcium ion do not change (NC) whilst those below either increase (I) or decrease (D) with increasing pressure. Note the dark blue and green spheres represent the manganese ions on the Mn1 and Mn2 crystallographic sites, the teal spheres represents the single Ca^{2+} crystallographic site and the red spheres represent the oxygen anions.Bottom Left: Variation in Ca–O1–Mn bond angles a function of pressure (Ca–O2–Mn1 - open squares and Ca–O2–Mn2 filled squares).Bottom Right: Variation in Ca–O1–Mn2 bond angle with pressure.

4. Conclusions

In summary we have investigated the pressure dependent behaviour of the layered oxide, $Ca_2Mn_3O_8$ at temperatures of 290 K and 120 K. These studies demonstrate that there is a smooth decrease in the lattice parameters and unit cell volume with increasing pressure. Compression of the structure is largely anisotropic and predominantly occurs in the interlayer direction(s) as opposed to the intralyer directions consistent with data reported for the compression of similar layered oxides [40, 43, 41, 42, 44, 45]. On the local scale compression behaviour is far more complex. Bond lengths and bond angle values suggest that there is little tilting or strain associated with the MnO_6 octahedra. In contrast the CaO_6 trigonal bipyramidal site becomes increasingly strained with increasing pressure. More over contraction appears to be driven by one side of the CaO_6 polyhedra with the other side remaining largely unchanged. The nature of the stucture means that this behaviour alternates between neighbouring Ca^{2+} which results in a shearing of the layers. These studies provide insight into the compression behaviour of $Ca_2Mn_3O_8$ which may be useful for optimising dopant (chemical pressure) studies as well as providing deeper understanding which will allow optimisation of this

material for application.

5. Acknowledgments

References

[1] R. Manickam, V. Yesuraj, K. Biswas, Doped CuCrO$_2$: A possible materialfor supercapacitor applications, Mater. Sci. Semicond. Process. 109 (2020) 104928.

[2] P. Beraslegui, C.-W. Tai, M. Valvo, Electrochemical reaction of AgFeO$_2$ as negative electrode in Li- and Na- ion batteries, J. Power Sources 401 (2018) 386–396.

[3] D. Nayak, P. K. Jha, S. Ghosh, V. Adyam, Aluminium substituted beta-type Na$_{1-x}$Al$_x$MnO$_2$: A stable and enhanced electrochemical kinetic sodium ion battery cathode, J. Power Sources 438 (2019) 227025.

[4] L. M. Zheng, Z. Q. Wang, M. S. Wu, B. Xu, C. Y. Ouyang, Jahn-Teller type small polaron assisted Na diffusion in NaMnO$_2$ as a cathode material for Na-ion batteries, J. Mater. Chem. A 7 (2019) 6053–6061.

[5] M. P. Down, E. Martinez-Perinon, C. W. Foster, E. Lorenzo, G. C. Smith, C. E. Banks, Next-generation additive manufacturing of complex standalone sodium-ion energy storage architectures, Adv. Energy Mater. 9 (2019) 1803019.

[6] M. Tato, R. Shironishi, M. Hagiwara, S. Fujihara, Reactive templated grain growth and thermoelectric power factor enhancement of textured CuFeO$_2$ ceramics, ACS Energy Mater. 3 (2020) 1979–1987.

[7] P. Yardanov, W. Sigle, P. Kaya, M. E. Gruner, R. Pentcheva, B. Keimer, H. U. Habermuer, Large thermopower anisotropy in PbCoO$_2$ thin films, Phys. Rev. Mater. 3 (2019) 085403.

[8] T. I. Draskovic, Y. Wu, Electrocatalytic properties of cuprous delafossite oxides for the alkaline oxygen reduction reaction, ChemCatChem 9 (2017) 3837–3842.

[9] Y. W. Deng, D. H. Xiong, H. Gao, J. Wu, S. K. Verma, B. S. Lutz, X. J. Zhao, Hydrothermal synthesis of delafossite CuScO$_2$ hexagonal plates as an electrocatalyst for the alkaline oxygen evolution reaction, Dalton Trans. 49 (2020) 3519–3524.

[10] F. Podjaski, D. Weber, S. Y. Zhang, L. Diehl, R. Eger, V. Duppel, E. Alarco-Llado, G. Richter, F. Haase, A. F. I. Morral, Rational strain engineering in deafossite oxides for highly efficient hydrogen evolution catalysis in acidic media, Nat. Catal. 3 (2020) 55–63.

[11] R. L. Dally, R. Chisnell, L. Harriger, Y. H. Liu, J. W. Lynn, S. D. Wilson, Thermal evolution of quasi-one-dimensional spin correlations within the anisotropic triangular lattice of alpha-NaMnO$_2$, Phys. Rev. B 98 (2018) 144444.

[12] F. Orlandi, E. Aza, I. Bakaimi, K. Kiefer, K. Klemke, B. Zorko, A. Arcon, C. Stock, G. D. Tsibidis, M. A. Green, P. Manuel, A. Lappas, Incommensurate atomic and magnetic modulations in the spin frustrated beta-NaMnO$_2$ triangular lattice, Phys. Rev. Mater. 2 (2018) 074407.

[13] A. Zorko, O. Adamopoulos, M. Komelj, D. Arcon, A. Lappas, Frustration-induced nanometre-scale inhomogenity in a triangular lattice, Nature Commun. 95 (2014) 3222.

[14] T. Nakajima, N. Terada, S. Mitsuda, R. Bewley, Spin driven bond order in a 1/5-magnetization plateau phase in the triangular lattice antiferromagnet CuFeO$_2$, Phys. Rev. B 88 (2013) 134414.

[15] T. Nakajima, A. Suno, S. Mitsuda, N. Terada, S. Kimura, K. Kaneko, H. Yamauchi, Magnons and electromagnons in a spin-lattice-coupled frustrated magnet CuFeO$_2$ as seen via inelastic neutron scattering, Phys. Rev. B 84 (2011) 184401.

[16] A. M. L. Lopes, G. N. P. Oliveira, T. M. Mendonca, J. A. Moreira, A. Almeida, J. P. Aravjo, V. S. Amaral, J. G. Correla, Local distortions in multiferroic AgCrO$_2$ triangular spin lattice, Phys. Rev. B 84 (2011) 014434.

[17] G. B. Ansell, M. A. Modrick, J. M. Longo, K. R. Poeppeimeler, H. S. Horowitz, Structure of calcium manganese oxide Ca$_2$Mn$_3$O$_8$, Acta Crystallographica Section B 38 (6) (1982) 1795–1797. doi:10.1107/S0567740882007201.
URL https://doi.org/10.1107/S0567740882007201

[18] H. S. Horowitz, J. M. Longo, Calcium manganese oxide, Ca$_2$Mn$_3$O−8, Inorg. Synth. 22 (1983) 73–XX.

[19] H. S. Horowitz, J. M. Longo, Phase relations in the Ca-Mn-O system, Mat. Res. Bull. 13 (1978) 1359–XX.

[20] T. R. White, W. S. Glaunsinger, H. S. Horowitz, J. M. Longo, Magnetic properties of the layered compounds Ca$_2$Mn$_3$O$_8$ and Cd$_2$Mn$_3$O$_8$, J. Solid State Chem. 29 (1979) 205.

[21] M. M. Najafpour, N. Pashaei, S. Nayeri, Calcium manganese(IV) oxides: biomimetic and efficient catalysts for water oxidation, Dalton Trans. 41 (2012) 4799.

[22] M. M. Najafpour, D. J. Sedigh, Water oxidation by manganese oxides, a new step towards a complete picture: simplicity is the ultimate sophistication, Dalton Trans. 42 (2013) 12173.

[23] A. Ramirez, P. Bogdanoff, D. Friedrich, S. Fiechter, Synthesis of Ca−2Mn_3O−8 films and their electrochemical studies for the oxygen evolution reaction (OER) of water, Nano Energy 1 (2012) 282.

[24] E. Braktash, I. Zaharieva, M. Schroder, C. Goebel, H. Dau, A. Thomas, Cyanamide route to calcium–manganese oxide foams for water oxidation, Dalton Trans. 42 (2013) 16920.

[25] X. Han, T. Zhang, J. Du, F. Cheng, Porous calcium–manganese oxide microspheres for electrocatalytic oxygen reduction with high activity, Chem. Sci. 4 (2013) 368.

[26] J. Yang, H. Yu, Y. Wang, F. Qi, H. Liu, L.-L. Lou, K. You, W. Zhou, S. Liu, Effect of Oxygen coordination environment of Ca-Mn oxides on the catalytic performance of Pd supported catalysts for aerobic oxidation of 5-hydroxymethyl-2-furfural, Catal. Sci. Technol. 9 (2019) 6659.

[27] A. Gagrani, M. Alsultan, G. F. Swigers, T. Tsuzuki, Comparitive evaluation of the structural and other features governing photoelectrochemical oxygen evolution by Ca/Mn oxides, Catal. 10 (2020) 2152.

[28] Y. J. Park, M. A. Doeff, Synthesis and electrochemical characterization of M$_2$Mn$_3$O−8 (M= Ca, Cu) compounds and derivatives, Solid State Ionics 177 (2006) 893–XX.

[29] L. J. Vera Stimpson, S. Ramos, G. B. G. Stenning, M. Jura, S. Parry, G. Cibin, D. C. Arnold, Investigation of the role of morphology on the magnetic properties of Ca$_2$Mn$_3$O$_8$ materials, Dalton Trans. 46 (2017) 14130.

[30] L. J. Vera Stimpson, E. E. Rodriguez, C. M. Brown, G. B. G. Stenning, M. Jura, D. C. Arnold, Magnetic ordering in a bow-tie lattice, J. Mater. Chem. C 6 (2018) 4541–4548.

[31] L. J. Vera Stimpson, J. A. McNulty, F. D. Morrison, , A. Mahajan, E. E. McCabe, A. S. Gibbs, G. B. G. Stenning, M. Jura, D. C. Arnold, A comprehensive variable temperature study of the layered oxide, Ca$_2$Mn$_3$O$_8$, J. Alloys Compd. X (2020) XXXX.

[32] J. Zhao, N. L. Ross, R. J. Angel, New view of the high-pressure behaviour of GdFeO$_3$-type perovskites, Acta Crystallographica Section B 60 (3) (2004) 263–271. doi:10.1107/S0108768104004276.
URL https://doi.org/10.1107/S0108768104004276

[33] T. Nakajima, Y. Iguchi, H. Tamatsukuri, S. Mitsuda, Y. Yanasami, H. Nakao, N. Terada, Uniaxial-pressure effects on spin-driven lattice distortions in geometrically frustrated magnets CuFe$_{1-x}$Ga$_x$O$_2$ ($x = 0$, 0.035), J. Phys. Soc. Jpn. 82 (2013) 114711.

[34] T. Nakajima, S. Mitsuda, K. Takahashi, K. Yoshitami, K. Masuda, C. Kaneko, Y. Honma, S. Kobayashi, H. Kitazawa, M. Kosaka, N. Aso, Y. Uwatoko, N. Terada, S. Wakimoto, M. Takeda, K. Kakurai, Uniaxial pressure control of magnetic phase transitions in a frustrated magnet CuFe$_{1-x}$Ga$_x$O$_2$ ($x = 0$, 0.018), J. Phys. Soc. Jpm. 81 (2012) 094710.

[35] H. Tamatsukuri, S. Mitsuda, T. Nakamura, K. Takata, T. Nakjima, K. Prokes, F. Yakaichiya, K. Kiefer, Spin-lattice-coupling-mediated magnetoferroelectric phase transition induced by uniaxial pressure in multiferroic CuFe$_{1-x}$$M_xO_2$ (M = Ga, Al), Phys. Rev. B. 95 (2017)

174108.

[36] T. Nakajima, S. Mitsuda, J. T. Haraldsen, R. S. Fishman, T. Hong, Y. Terada, N. Uwatoko, Magnetic interation in the multiferroic phase of CuFe$_{1-x}$Ga$_x$O$_2$ ($x = 0.035$) refined by inelastic neutron scattering with uniaxial-pressure control of domain structure, Phys. Rev. B. 85 (2012) 144405.

[37] T. Nakajima, S. Mitsuda, T. Nakamura, H. Ishii, T. Haku, Y. Honma, M. Kosaka, N. Aso, Y. Uwakoto.

[38] N. Terada, N. Qureshi, L. C. Chapon, T. Osakabe, Spherical neutron polarimetry under high pressure for a multiferroic ferite, Nature Commun. 9 (2018) 4368.

[39] W. M. Xu, G. R. Hearne, M. P. Pasternak, CuFeO$_2$ at a megabar: Stabilisation of a mixed-valence low-spin magnetic semiconducting ground state, Phys. Rev. B. 94 (2016) 035155.

[40] J. Pellier-Porres, A. Segura, C. Ferrer-Roca, D. Martinez-Garcia, J. A. Sans, E. Martinez, J. P. Itie, A. Polian, F. Baudelet, A. Munoz, P. Rodriguez-Hernandez, P. Munsch, Structural evolution of CuGaO$_2$ delafossite under high pressure, Phys. Rev. B. 69 (2004) 024109.

[41] M. Hasagawa, M. Tanaka, T. Yagi, H. Takei, A. Inoue, Compression behaviour of the delafossite-type metallic oxide PbCoO$_2$ below 10 GPa, Solid State Commun. 128 (2003) 33.

[42] W. M. Xu, G. K. Rozenberg, M. P. Pasternak, M. Kertzer, A. Kurnosov, L. S. Dubrovinsky, S. Pascarelli, M. Munoz, M. Vaccari, M. Hanfland, R. Jeanloz, Pressure-induced Fe↔Cu cationic valence exchange and its structural consequences: high-pressure studies of delafossite CuFeO$_2$, Phys. Rev. B. 81 (2010) 104110.

[43] A. Pellier-Porres, A. Segura, C. Ferrer-Roca, P. Munsch, D. Kim, XRD and XAS structural study of CuAlO$_2$ under high pressure, J. Phys.:Condens. Matter. 25 (2013) 115406.

[44] T. R. Zhao, M. Hasegawa, H. Takei, T. Kondo, T. Yagi, High pressure x-ray diffraction study of CuFeO$_2$, Jpn. J. Appl. Phys. 35 (1996) 3535.

[45] T. R. Zhao, M. Hasegawa, T. Kondo, T. Yagi, H. Takei, X-ray diffraction study of copper iron oxide [CuFeO$_2$] under pressures up to 10 GPa, Mat. Res. Bull. 32 (1997) 151.

[46] N. Terada, D. D. Khalyavin, P. Manuel, T. Osakabe, P. G. Radaelli, H. Kitazawa, Pressure-induced polar phases in multiferroic delafossite CuFeO$_2$, Phys. Rev. B. 89 (2014) 220403.

[47] A. Miura, M. Wessel, R. Dronskowski, Calculation of the electronic-structure of delafossite AgTaN$_2$ from first principles, J. Ceram. Soc. Jpn. 119 (2011) 663.

[48] A. Nakanishi, H. Katayama-Yoshida, Pressure induced structural transition and enhancement of energy gap in CuAlO$_2$, J. Phys. Soc. Jpn. 80 (2011) 024706.

[49] D. Upadhyay, A. Piatap, P. K. Jha, A first principles study on structural dynamical and mechanical stability of newly predicted delafossite HCoO$_2$ at high pressure, J. Raman Spec. 50 (2019) 603.

[50] J. Pellicer-Porres, A. Segura, E. Martinez, A. M. Saitta, A. Polian, J. C. Cherun, B. Canny, Vibrational properties of delafossite CuGaO$_2$ at ambient and high pressures, Phys. Rev. B. 72 (2005) 064301.

[51] H. Tamatsukuri, S. Mitsuda, T. Shimizu, M. Fujihala, H. Yokota, K. Takehara, Y. Imariaka, A. Nakao, K. Munakata, Nonlinear piezomagnetoelectric effect of CuFeO$_2$, Phys. Rev. B. 100 (2019) 201105.

[52] C. L. Bull, N. P. Funnell, M. G. Tucker, S. Hull, D. J. Francis, W. G. Marshall, PEARL: the high pressure neutron powder diffractometer at ISIS, High Pressure Research 36 (4) (2016) 493–511. doi:10.1080/08957959.2016.1214730.
URL http://dx.doi.org/10.1080/08957959.2016.1214730

[53] W. G. Marshall, D. J. Francis, Attainment of near-hydrostatic compression conditions using the Paris-Edinburgh cell, J. Appl. Crystallogr. 35 (2002) 122–125.

[54] J. M. Besson, R. J. Nelmes, G. Hamel, J. S. Loveday, G. Weill, S. Hull, Neutron powder diffraction above 10 GPa, Physica B 180 (1992) 907–910.

[55] O. Arnold, J. C. Bilheux, J. M. Borreguero, A. Buts, S. I. Campbell, L. Chapon, M. Doucet, N. Draper, R. Ferraz Leal, M. A. Gigg, V. E. Lynch, A. Markvardsen, D. J. Mikkelson, R. L. Mikkelson, R. Miller, K. Palmen, P. Parker, G. Passos, T. G. Perring, P. F. Peterson, S. Ren, M. A. Reuter, A. T. Savici, J. W. Taylor, R. J. Taylor, R. Tolchenov, W. Zhou, J. Zikovsky, Mantid—Data analysis and visualization package for neutron scattering and μSR experiments, Nucl. Instrum. Meth. A 764 (2014) 156–166. doi:http://dx.doi.org/10.1016/j.nima.2014.07.029.
URL http://www.sciencedirect.com/science/article/pii/S0168900214008729

[56] B. H. Toby, EXPGUI, a graphical user interface for GSAS, J. Appl. Crystallogr. 34 (2) (2001) 210–213. doi:10.1107/S0021889801002242.
URL http://dx.doi.org/10.1107/S0021889801002242

[57] A. C. Larson, R. B. Von Dreele, General Structure Analysis System (GSAS), Los Alamos National Laboratory Report (LAUR) 86 (2004) 748.

[58] S. Klotz, J. C. Chervin, P. Munsch, G. L. Marchand, Hydrostatic limits of 11 pressure transmitting media, J. Phys. D: Appl. Phys. 42 (2009) 075413.

[59] A. D. Fortes, Revised equation of state for in situ pressure determination using fcc-pb (0p13 gpa, t100 k, RAL Technical Reports RAL-TR-2019-002 (2019).

[60] M. J. Cliffe, A. L. Goodwin, PASCal: a principal axis strain calculator for thermal expansion and compressibility determination, Journal of Applied Crystallography 45 (6) (2012) 1321–1329.

[61] D. C. Arnold, C. L. Bull, Pressure driven phase transitions in the magnetically frustrated layered material, Ca$_2$Mn$_3$O$_8$, 10.5286/ISIS.E.RB1930086 (2019).